Springer

Acta Mechanica Sinica

CrossMark click for updates

• RESEARCH PAPER •

Acta Mech. Sin., Vol. 41, 524251 (2025)
https://doi.org/10.1007/s10409-024-24251-x

Aircraft propeller erosion wear and aerodynamic characteristics

Xiangying Guo, Fujin Zang, Yunan Zhu, and Dongxing Cao*

Beijing Key Laboratory of Nonlinear Vibrations and Strength of Mechanical Structures, College of Mechanical Engineering, Beijing University of Technology, Beijing 100124, China

Received May 28, 2024; accepted June 5, 2024; published online August 27, 2024

This study investigates surface erosion wear caused by collision and friction between propellers and sand particles during the flight of propeller transport aircraft in harsh environments like deserts and plateaus, which are characterized by strong sand and wind conditions. Firstly, the erosion behavior of individual propeller blades is analyzed under various sand particle parameters using the commercial software FLUENT. Subsequently, dynamic simulations of the entire blade are conducted by the sliding mesh method to examine erosion patterns under different operational conditions, including rotation speed and climb angle. Finally, the impact of erosion on the aerodynamic characteristics of the propeller is obtained based on simulation results. This study delves into the erosion patterns observed in large aircraft propellers operating within sandy and dusty environments, as well as the consequential impact of propeller surface wear on aerodynamic performance. By elucidating these phenomena, this research provides valuable insights that can inform future endeavors aimed at optimizing propeller design.

Aircraft propellers, Erosive wear behavior, Aerodynamic characteristics

Citation: X. Guo, F. Zang, Y. Zhu, and D. Cao, Aircraft propeller erosion wear and aerodynamic characteristics, Acta Mech. Sin. 41, 524251 (2025), https://doi.org/10.1007/s10409-024-24251-x

1. Introduction

In low-altitude operations of aircraft in high-wind and sandstorm environments such as plateaus and deserts, erosion by sand particles emerges as an inevitable challenge owing to environmental factors [1]. Generally, the turbulent airflow generated by rotor blades results in the ingestion of sand particles into the rapidly rotating blade area, consequently leading to erosive wear [2] which can be described by solid particle erosion. Since erosive wear can affect propeller-airframe interactions and result in the worsening of aerodynamic performance, it is important to investigate the erosive wear behavior of aircraft propellers for enhancing aircraft performance and safety in harsh environments.

Numerous scholars have endeavored to elucidate the erosion mechanisms of high-speed rotating blades and variously shaped target materials through experimental and simulation studies. In the initial phases of research, scholars like Hutchings [3], Oka and Yoshida [4] introduced theoretical models that accounted for multiple factors to forecast the erosive wear attributes of metal surfaces induced by particles. Shin et al. [5] conducted solid particle erosion experiments on helicopter rotors in conditions of low-altitude dense particles, revealing elevated erosion levels at the blade tips. Additionally, Liu et al. [6] explored the effects of impact velocity and angle of spherical and sharp-edged geometric particles on erosion, with numerical simulation results corroborating experimental findings. With the growing application of composite materials in aviation, land transportation, and industrial sectors, the erosive behavior of composite materials had garnered considerable attention [7-11]. Özen et al. [12] conducted numerical simulations on the erosive behavior of various skin materials on helicopter rotor blades, obtaining insights into the erosion resistance characteristics of different materials. However, researches on the erosive wear of propeller blades are relatively scarce.

To date, most studies on erosive wear have focused on engine rotor blades, given their pivotal role in engine thrust and fuel consumption, such as Li et al. [13-15] experimentally derived key parameters of the Finnie erosion model and

*Corresponding author. E-mail address: caostar@bjut.edu.cn (Dongxing Cao)
Executive Editor: Zhixiang Xiao

investigated the erosive wear patterns of aviation turbo-shaft engine blades, alongside the unbalanced vibration characteristics caused by erosion. Results showed the differences in erosion distribution and severity between distorted and non-distorted regions. Ghenaiet et al. [16] delved into particle injection and blade erosive wear rates in the first-stage axial compressor of a specific turbofan engine, predicting trends in blade thickness variation under extreme conditions. Dong et al. [17,18] developed a gridless model capable of simulating various geometric particle shapes, replicating material removal behaviors under different particle shapes. Suzuki and Yamamoto [19] examined erosive wear on a single-stage axial compressor, identifying abrasive wear on the leading edge and pressure surface of compressor blades as the primary causes of blade failure.

Insufficient surface protection of turbine blades leads to damage due to erosion, altering the aerodynamic characteristics of the blades and diminishing turbine performance [20]. Corsini et al. [21] found that the geometric shape of turbine blades influences their aerodynamic effects differently, resulting in varied erosion distributions at the same power output and operating points. When aircraft rotor blades are subjected to erosion due to particle impacts during high-speed rotation, the aerodynamic performance of the rotor blades is adversely affected by erosive damage. Hence, an investigation into the erosion mechanism affecting the surface of rotor blades due to particle interaction was conducted in this scenario [22-26].

In recent years, computational fluid dynamics (CFD) has been widely applied in analyzing erosion processes occurring on object surfaces. Erosion analysis based on CFD offers significant advantages for complex surface geometries and different operating conditions [27-33]. In the study of erosion on the leading edge of engine blades, CFD-based analysis and simulation have been widely employed [34-36]. This approach is also employed to study the erosion of wind turbine blades in challenging environmental conditions. The blades of wind turbines undergo erosion and damage from heavy rain and sandstorms, leading to a significant impact on their operational efficiency [37,38].

Therefore, this work is to investigate the erosive wear of aircraft propeller blades in sandstorms working environments and explore the aerodynamic performance losses induced by erosive wear of propeller blades. Firstly, the erosive conditions under different particle parameters are analyzed. Then, transient simulations are performed to simulate erosion mechanisms under varying speeds and climbing angles in realistic environments. Based on the obtained erosive conditions of propeller blades, roughness is applied to severe erosion areas to explore the influence of erosion-induced surface roughness on aerodynamic performance. This study will provide theoretical guidance for subsequent erosion-resistant research endeavors.

2. Numerical analysis

2.1 Mathematical model

In this study, numerical simulations were conducted using the commercial software Ansys-Fluent, based on CFD. The erosion analysis encompasses solving flow equations, particle motion equations, and calculating the erosion rate on the object's surface. Key methodologies employed include the discrete phase model (DPM), the sliding mesh method, and the multiple reference frame (MRF) approach.

Here, mass and momentum conservation equations are applied to determine flow characteristics of the particles and the Navier-Stokes equations are used for solving momentum and energy conservation equations of the particles. The generalized state equations of the Reynolds averaged Navier-Stokes (RANS) are provided by Eqs. (1) and (2):

$$\frac{\partial \rho}{\partial t}+\frac{\partial}{\partial x_i}(\rho U_i)=0, \tag{1}$$

$$\frac{\partial}{\partial t}(\rho U_i)+\frac{\partial}{\partial x_i}\left(\rho U_i U_j\right) = -\frac{\partial P}{\partial x_i}+\frac{\partial}{\partial x_j}\left[\mu\left(\frac{\partial U_i}{\partial x_j}+\frac{\partial U_j}{\partial x_i}-\frac{2}{3}\delta_{ij}\frac{\partial u_k}{\partial x_k}\right)\right]+\frac{\partial}{\partial x_i}\left(-\rho\overline{u_i' u_j'}\right), \tag{2}$$

where ρ is the fluid density, P is the pressure, μ is the dynamic viscosity of air, δ_{ij} is the Kronecker-Delta operator, U_i and U_j are the velocity of air, and $-\rho\overline{u_i' u_j'}$ is the Reynolds stress.

In this study, both the particles and all walls are considered adiabatic, hence thermal exchange is not accounted for in the simulation calculations, eliminating the need to solve energy equations. Since the momentum equation for the turbulence model requires closure, the employed model is the standard k-ε model, with its governing equations as follows [39]:

$$\frac{\partial \rho k_t U_i}{\partial x_i}=\frac{\partial}{\partial x_j}\left[\left(\mu+\frac{C_\mu P k_t^2}{\varepsilon\sigma_k}\right)\frac{\partial U_i}{\partial x_i}\right]+G_k-\rho\varepsilon, \tag{3}$$

$$\frac{\partial \rho \varepsilon U_i}{\partial x_i}=\frac{\partial}{\partial x_j}\left[\left(\mu+\frac{C_\mu \rho k_t^2}{\varepsilon\sigma_\varepsilon}\right)\frac{\partial U_i}{\partial x_i}\right]+\frac{C_{1\varepsilon}\varepsilon}{k_t}G_k-C_{2\varepsilon}\rho\frac{\varepsilon^2}{k_t}, \tag{4}$$

where k_t is the turbulent kinetic energy, μ is the dynamic viscosity, ε refers to the turbulent dissipation rate, G_k is the generation term of turbulent kinetic energy, σ_k is the turbulent Prandtl number, and $C_{1\varepsilon}$, $C_{2\varepsilon}$, C_μ and σ_ε are the empirical parameters obtained from experimental tests, which are 1.44, 1.92, 0.09 and 1.3, respectively.

In Fluent, particle erosion is simulated using the discrete phase model (DPM), where particle tracking is conducted via the Lagrangian method. The approach is characterized by a one-way coupling. which can track the motion of the particles and incorporate the collision data of these particles into an erosion equation. Therefore, the primary particle

motion equation employed in Fluent is as follows [40]:

$$\frac{\mathrm{d}V_P}{\mathrm{d}t} = F_D(U - V_P) + \frac{g(\rho_p - \rho)}{\rho_P} + F_R. \tag{5}$$

In the above formula,

$$F_D = \frac{18\mu C_D Re}{\rho_P d_p^2 \cdot 24}, \tag{6}$$

where F_D is the drag force per unit mass of the particle, U is fluid velocity, V_P is velocity, ρ_P is particle density, g is gravitational acceleration, d_P is particle diameter, C_D is drag coefficient, F_R is other forces per unit mass, and R_e is relative Reynolds number.

Erosion wear is a phenomenon characterized by the erosion or wear of solid particles or fluids, which is primarily induced by the surface properties of the materials. The wear rate is a commonly used metric to quantify the extent of material degradation and can be represented by the following equation [41]:

$$R_{\text{erosion}} = \sum_{P=1}^{N_P} \frac{m_p C(d_p) f(\alpha) v^{b(v)}}{A_{\text{face}}}, \tag{7}$$

where m_p is particle quality; $C(d_P)$ is particle diameter function; α is particle impact material surface angle; $f(\alpha)$ is impact angle function; v is particle impact relative speed; $b(v)$ is relative speed function; A_{face} is particles on the surface of the material erosion wear area; and N_P is the number of particles hitting the material at the wear.

When numerically simulating roughness using the CFD method in Fluent, the concept of equivalent particle roughness K_s^+ is employed, which involves overlaying a layer of closely arranged, uniformly sized spherical particles on the blade surface. K_s^+ is utilized to characterize the surface roughness of the blade and is defined as follows:

$$K_s^+ = \frac{\rho K_s u^*}{\mu}, \tag{8}$$

where ρ represents the air density, u^* denotes the wall friction velocity, μ stands for the fluid dynamic viscosity coefficient, and K_s is the equivalent particle roughness height.

The expression for K_s is as follows:

$$K_s = \frac{3M_e}{2S_e\rho_L}, \tag{9}$$

where M_e represents the erosion mass, S_e denotes the erosion area, and ρ_L stands for the density of the propeller skin material.

In addition, it involves some parameters of the propeller, which exert a direct influence on the efficiency and efficacy of aircraft operations. Here, two parameters are considered, including the thrust coefficient C_T and power coefficient C_P, which stand as a comprehensive portrayal of its thrust generation capabilities and power consumption characteristics. The pertinent calculation formulas are delineated below:

$$C_T = \frac{T}{\rho n^2 D^4}, \tag{10}$$

$$C_P = \frac{P}{\rho n^3 D^5}, \tag{11}$$

where T is the thrust, P is the power, ρ is the air density, n is the rotational speed, and D is the propeller diameter.

2.2 CFD Setup

This research investigates the impact of erosion wear on the propeller blades of large turboprop transport aircraft operating in desert environments. The simulation utilizes a propeller blade model derived from the JL-4A/1 type propeller, incorporating detailed geometric characteristics as illustrated in Fig. 1. The propeller boasts a substantial 4-meter diameter and is equipped with six blades. The propeller hub is constructed from aluminum alloy, while the blades are composed of composite materials. The blade angle is set at 30°, with a pitch measuring 7.176 m and a torque output of 48000 N·m. The model's development is facilitated by SolidWorks 2022 software, executed at a precise 1:1 scale.

The propeller blades exhibit a complex structure, featuring an outer protective coating and an inner composite structure. Erosion during propeller operation predominantly affects the outer protective coating. Initially, the propeller blade model is imported into Ansys-Fluent to create the model file. Subsequently, the external fluid domain of the propeller is defined, and the rotating region is partitioned and meshed. Concurrently, boundary conditions for the model are specified, as illustrated in Fig. 2.

To maintain computational precision, it is essential to represent model features with meshes of adequate fineness during the grid partitioning process. However, given the dimensional constraints of the propeller, the blade edge necessitates even finer mesh partitioning. Consequently, localized mesh refinement is implemented specifically on the blade edge of the propeller, as demonstrated in Fig. 3.

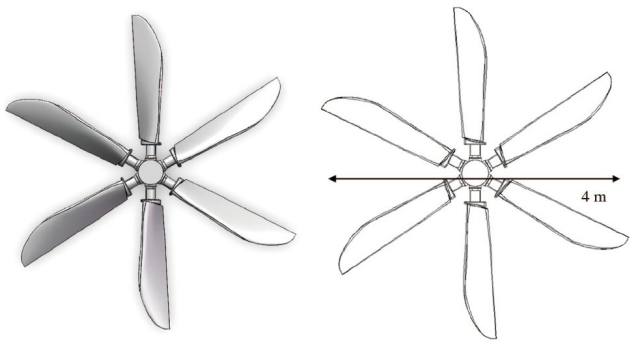

Figure 1 Propeller model.

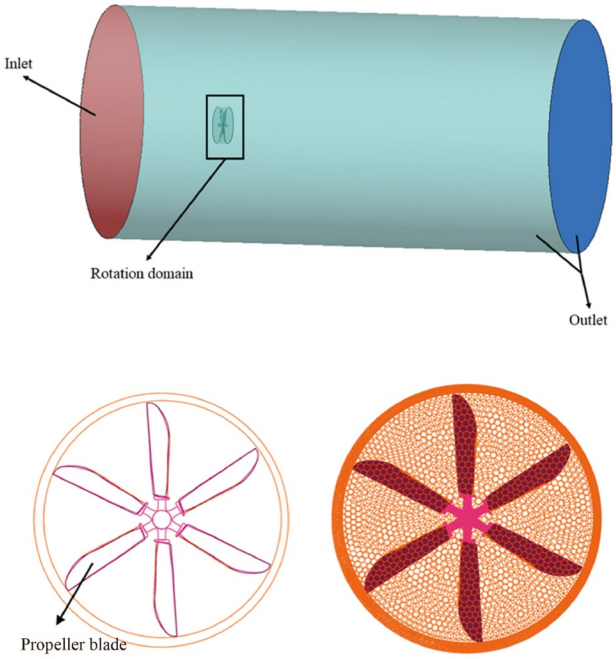

Figure 2 Fluid domain division and boundary conditions.

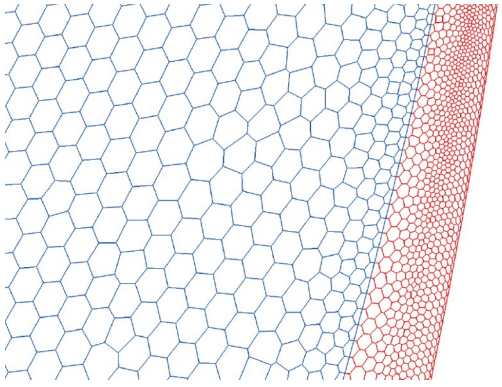

Figure 3 Local grid refinement: blade edge.

The mesh size on the pressure surface of the propeller blade has been designated as 5 mm, whereas a finer mesh size of 2 mm has been employed to more accurately capture the intricate features along the blade's edge.

In this simulation, Fluent Meshing was utilized to discretize the mesh of the external flow field, rotating domain, and propeller blades. A polyhedral mesh, renowned for its exceptional convergence characteristics, was selected. The model's composition encompassed a total of 5,584,633 elements, a configuration deemed sufficient for the objectives of this investigation, considering the specific model and mesh employed. Furthermore, an exploration of the model's mesh independence was undertaken by augmenting the element count. Table 1 presents the grid independence test conducted by increasing the number of elements, where ΔE_A represents the average erosion rate error under the same conditions. Upon comparing the results in the table, it is observed that increasing the number of grids has a negligible impact on the simulation outcomes, with errors remaining below 5%. Given this small margin of error, the grid quantity of 5,584,633 demonstrates time-saving advantages, leading us to deem it suitable for simulation in this study.

Table 1 Grid-independent verification

n	Number of elements	ΔE_A (%)
1	5,584,633	–
2	8,734,662	1.3%
3	12,076,331	2.1%

3. Results and discussion

3.1 Propeller parameter analysis

In operational settings like deserts and plateaus, aircraft are subjected to heightened exposure to sand dust particles, particularly during takeoff and climb phases. Incomplete statistics suggest that surface erosion resulting from the abrasive impact of wind and sand particles on propeller blades poses a significant threat not only to the longevity of the propeller but also to its overall performance. This section investigates the erosion wear experienced by propellers during takeoff under varying climb attitudes of the aircraft.

Transient solutions were derived using sliding mesh techniques while adjusting the propeller's climb angles (0°, 5°, 10°, 15°). Meanwhile, particle diameters were set to be randomly distributed from 100 μm to 500 μm.

Figures 4 and 5 provide contour maps and scatter plots illustrating erosion wear on propellers at different climb angles, respectively, with Table 2 presenting the corresponding average erosion rates of the blades. Comparative analysis reveals that as the climb angle increases, the erosion area on the propeller blades gradually expands from the blade tip to encompass the entire blade surface, leading to a widening of the erosion region and a concurrent reduction in average erosion rates. As shown in Fig. 5, the primary erosion rates of the blades are all concentrated below 4×10^{-5}.

The selection of rotational speeds (500 r/min, 800 r/min, and 1000 r/min) in this study was informed by the 4-meter diameter of the propeller model, ensuring the blades operated within a safe range.

Figures 6 and 7 depict contour maps and scatter plots illustrating erosion patterns on propeller blades at varying rotational speeds, respectively. Additionally, Fig. 8 presents erosion waterfall plots for a single blade at different locations, derived from surface data collected from corresponding positions on erosion contour maps. Table 3 complements these visuals by presenting the corresponding average erosion rates.

Comparative analysis of the results indicates that with increasing rotational speed, the erosion pattern shifts from a

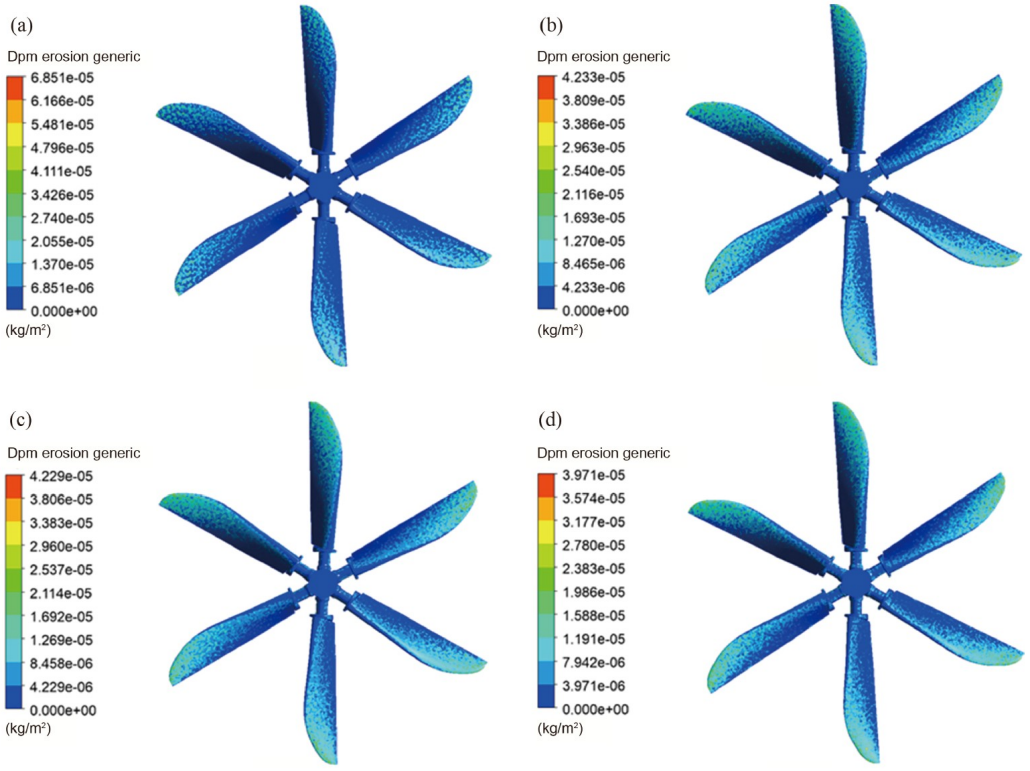

Figure 4 Different climb angles: (a) 0°; (b) 5°; (c) 10°; (d) 15°.

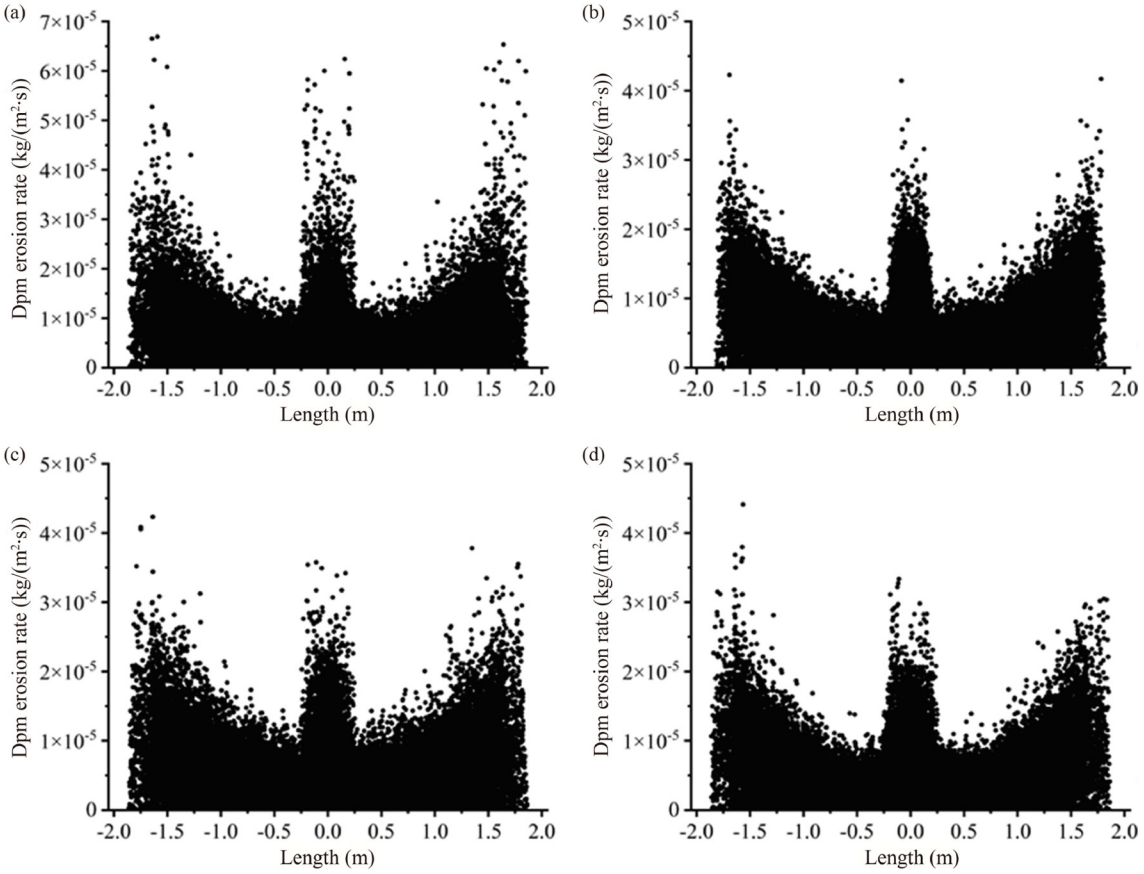

Figure 5 Scatterplot of erosion: (a) 0°; (b) 5°; (c) 10°; (d) 15°.

Table 2 Average erosion rate: different climb angles

Climb angle	E_A (kg/m^2)	Δ%
0°	2.94489×10^{-6}	–
5°	2.872606×10^{-6}	−2.5%
10°	2.814226×10^{-6}	−4.6%
15°	2.644134×10^{-6}	−11.4%

dispersed distribution across the blade surface, as observed in Figs. 6 and 8, to a concentration primarily at the blade edge and tip. In Fig. 8, the areas with prominent elevations correspond to the pressure surface and leading edge, while the flattened regions indicate the suction side of the blade. The data suggest that as the rotational speed increases, these elevated areas converge towards the sides and gradually intensify. This observation is consistent with the erosion distribution changes depicted in Fig. 6 and erosion rates at three rotational speeds shown in Fig. 7, primarily concentrated below 4×10^{-5}, 4.5×10^{-5}, and 8×10^{-5}, respectively. Moreover, it supports the findings presented in Table 3 which demonstrate an increase in erosion degree with rising rotational speed.

3.2 Particle parameter analysis

The preceding section conducted a comprehensive analysis of the impact of diverse operational parameters of the propeller on blade erosion, employing controlled manipulation. Conversely, the current section is dedicated to scrutinizing the influence of inherent particle parameters (particle diameter, incidence velocity, mass flow rate) on propeller blade erosion.

In this part, the effects of different factors on propeller blade erosion are investigated under realistic conditions. Firstly, typical particle sizes of different sand dust particles (100 μm, 300 μm, 500 μm) are selected on propeller blade erosion. The particles are introduced at the inlet depicted in Fig. 2, with a velocity of 50 m/s and a mass flow rate of 0.5 kg/s. To better replicate real-world scenarios, the computation considers the interaction between gas and solid phases, assuming no slip velocity between gas and particles. The erosion rate contour maps resulting from the computations are depicted in Fig. 9.

As depicted in Fig. 9, the regions of the blade edge and tip manifest the most pronounced erosion wear. Subsequent data processing of the propeller blade surface produced the erosion scatter distribution are illustrated in Fig. 10 and the corresponding average erosion rate is outlined in Table 4. Among these, the main erosion rates of the blade are predominantly concentrated below 3×10^{-10}. All of them indicate that an escalation in particle size correlates with a reduction in the maximum erosion rate, juxtaposed with an augmentation in the average erosion rate. This trend is ascribed to alterations in the airborne particle distribution accompanying variations in particle size. Larger particles are predisposed to adhering to individual propeller blade surfaces, prompting localized erosion zones and subse-

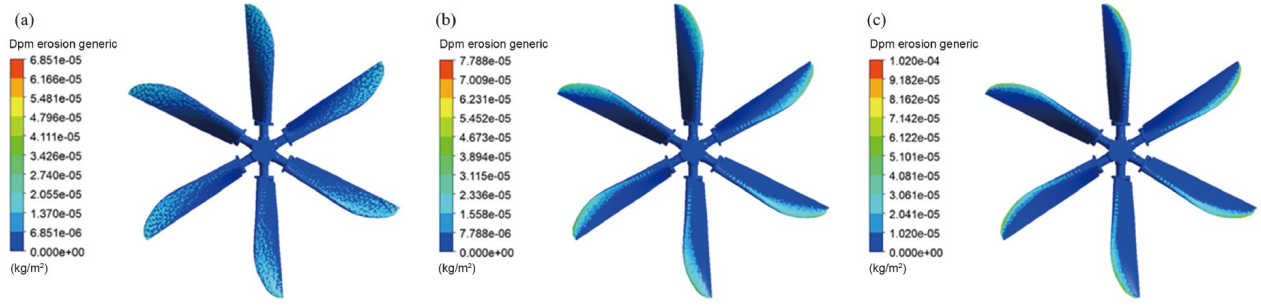

Figure 6 Different speeds: (a) 500 r/min; (b) 800 r/min; (c) 1000 r/min.

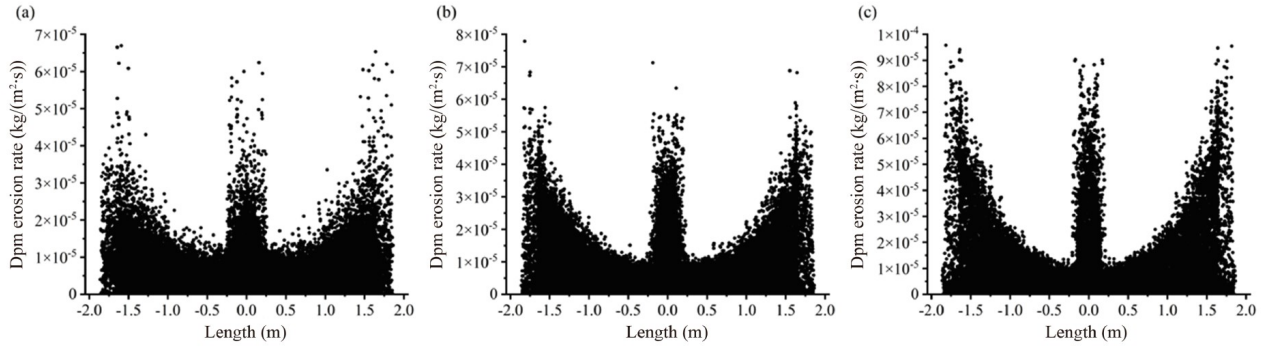

Figure 7 Scatterplot of erosion: (a) 500 r/min; (b) 800 r/min; (c) 1000 r/min.

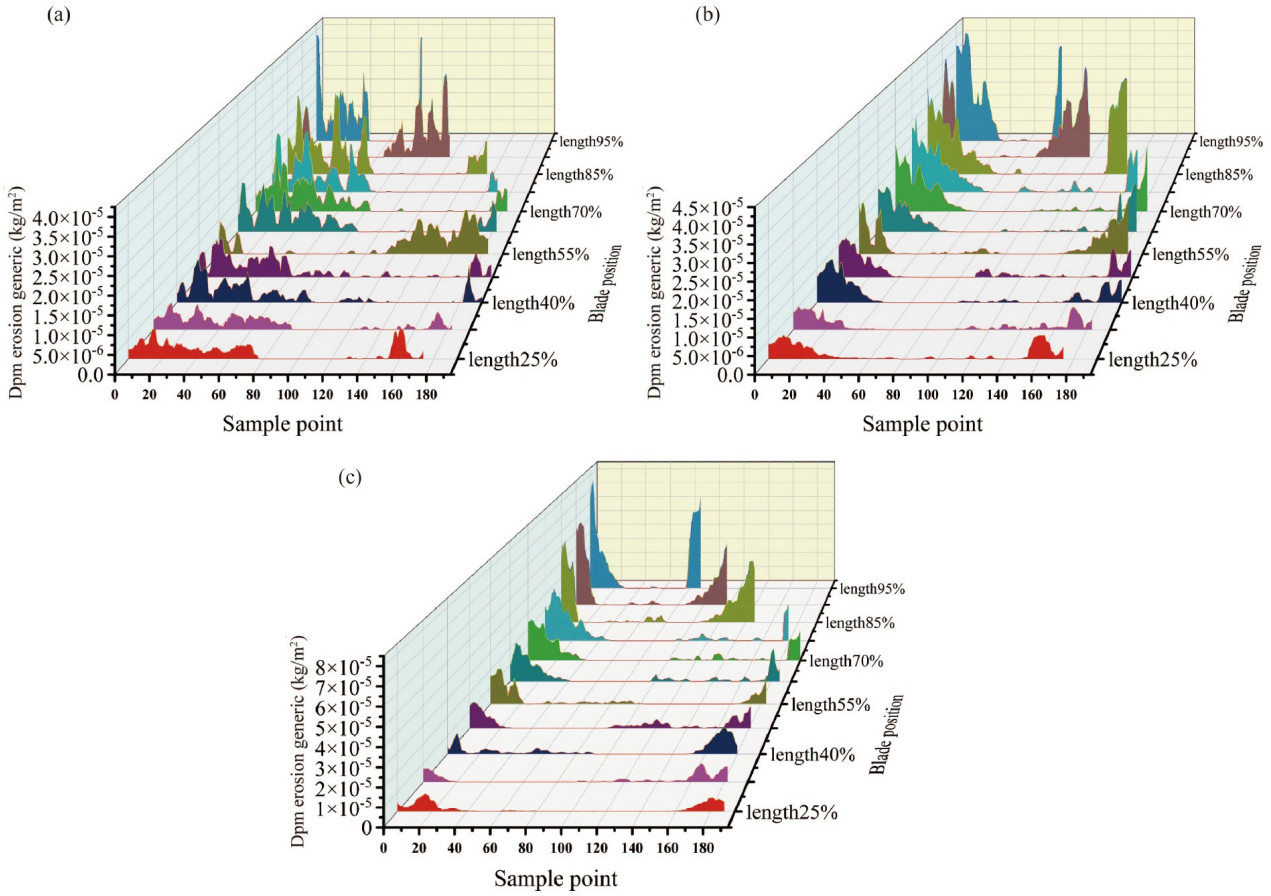

Figure 8 Waterfall plot: (a) 500 r/min (b) 800 r/min (c) 1000 r/min.

Table 3 Average erosion rate: different rotation speed

Rotation speed (r/min)	E_A (kg/m^2)	Δ%
500	2.94489×10^{-6}	–
800	3.2060756×10^{-6}	8.70%
1000	3.742729×10^{-6}	27.10%

quently diminishing the maximum erosion rate. In contrast, this uneven particle deposition will lead to foster an increase in the average erosion rate.

Figure 11 illustrates the distribution of erosion at various particle inlet velocities (50 m/s, 80 m/s, 100 m/s). Upon comparing the contour maps, it is evident that the primary erosion zones remain concentrated at the blade edge and tip. Further analysis involves processing the data from the blade surface, resulting in erosion scatter plots and average erosion rates depicted in Fig. 12 and Table 5, respectively. Among these, the main erosion rates of the blade are predominantly concentrated below 4×10^{-10}. The analysis indicates a direct correlation between the increase in particle inlet velocity and the overall rise in erosion levels. This phenomenon can be attributed to the heightened kinetic energy of the particles at increased flight velocities, leading to more vigorous energy transfer upon collision and consequently, more pronounced erosion.

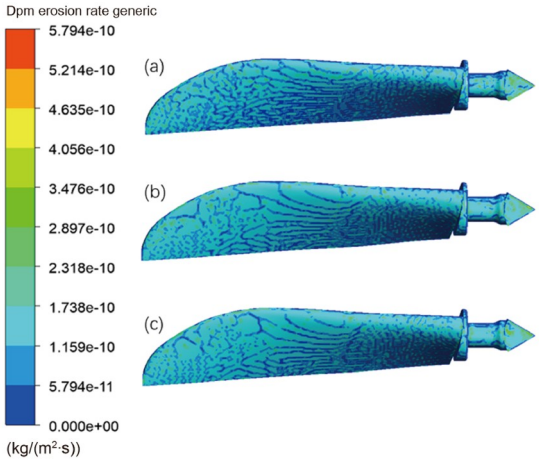

Figure 9 Propeller blade erosion at different grain sizes: (a) 100 μm; (b) 300 μm; (c) 500 μm.

Figure 13 illustrates the distribution of erosion on propeller blades across varying particle mass flow rates (0.5 kg/s, 0.8 kg/s, 1.0 kg/s). The data processing of the blade surfaces yields erosion scatter plots corresponding to each mass flow rate, as depicted in Fig. 14. The main erosion rates of the blade are predominantly concentrated below 3×10^{-10}, with average erosion rates tabulated in Table 6.

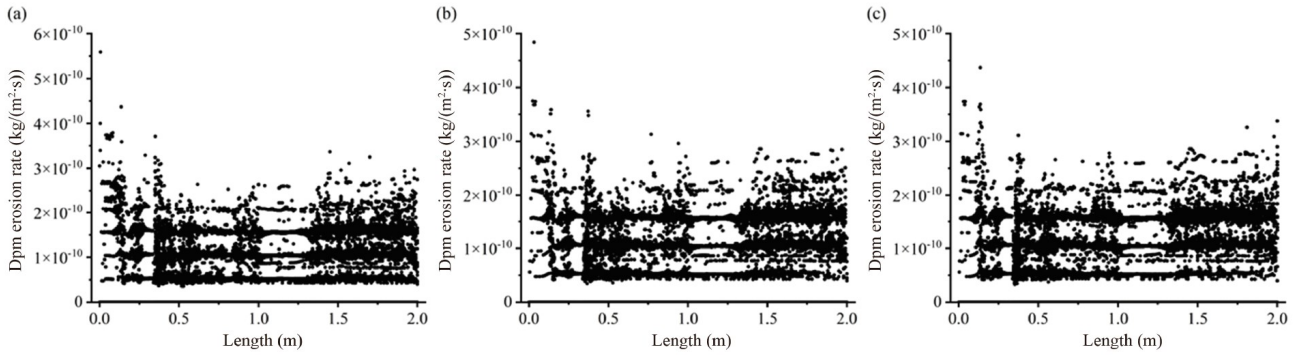

Figure 10 Scatterplot of erosion: (a) 100 μm; (b) 300 μm; (c) 500 μm.

Table 4 Average erosion rate: different grain sizes

Particle diameter (μm)	E_A (kg/(m^2·s))	Δ%
100	4.664935×10^{-11}	–
300	5.135014×10^{-11}	10.10%
500	5.256223×10^{-11}	12.70%

It indicates persistent concentration of erosion primarily at the blade's edge and tip and an increase in particle mass flow rate correlates with heightened erosion levels. This phenomenon can be ascribed to the augmented particle concentration, resulting in a greater number of collisions with the propeller surface per unit time, thus leading to more frequent particle impacts. Notably, a comparison of the three operational conditions highlights that variations in particle mass flow rate exert the most significant influence on erosion.

Through a comprehensive examination of various particle parameters, the erosion-wear characteristics affecting propeller blades were systematically investigated. Analysis presented in Table 7 clearly indicates that the augmentation of mass flow rate manifests as the primary influencing factor on propeller blade erosion, evidenced by a twofold increase in the average erosion rate when the mass flow rate escalates from 0.5 kg/s to 1 kg/s. In contrast, the alteration in particle impact velocity exerts minimal influence on the average erosion rate, with a negligible change of less than 1% observed upon velocity augmentation. Additionally, the significance of particle diameter on erosion rate cannot be understated, as its escalation similarly contributes to erosion rate amplification.

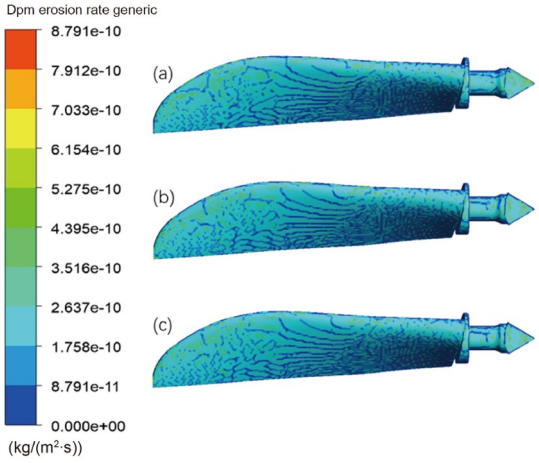

Figure 11 Different particle incidence velocities: (a) 50 m/s; (b) 80 m/s; (c) 100 m/s.

3.3 Aerodynamic and roughness analysis

The investigations conducted in Sects. 3.1 and 3.2 have shed light on the erosion patterns of propeller blades across diverse operational scenarios. It is observed that the primary erosion regions of the blades are predominantly concentrated at the blade tip and edge on the pressure side.

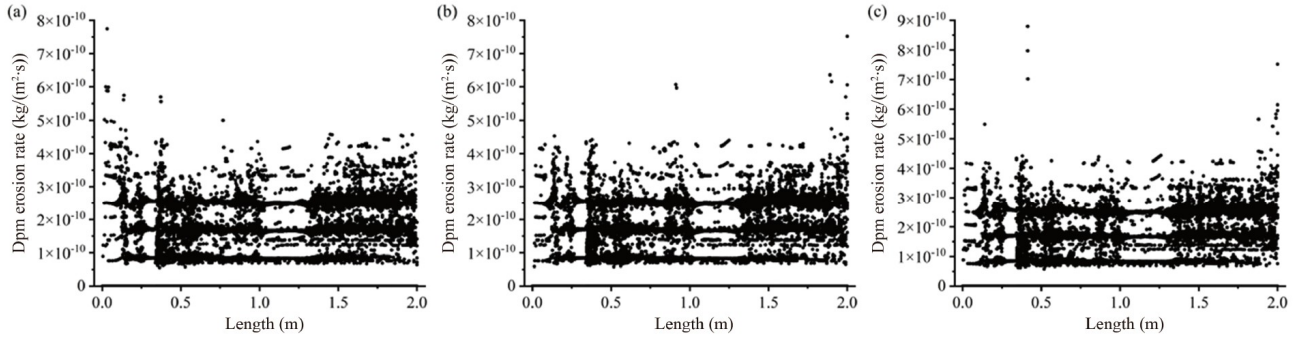

Figure 12 Scatterplot of erosion: (a) 50 m/s; (b) 80 m/s; (c) 100 m/s.

Table 5 Average erosion rate: different particle incidence velocities

Incidence velocity (m/s)	E_A (kg/(m^2·s))	Δ%
50	8.2141783×10^{-11}	–
80	8.2311689×10^{-11}	0.20%
100	8.2845971×10^{-11}	0.90%

Moreover, with increasing rotational speed, there is a tendency for the erosion area to transition from a dispersed distribution to a more localized one.

This section endeavors to delve into the performance deterioration of the propeller resulting from this phenomenon by scrutinizing the impact of erosion on its aerodynamic efficiency, specifically focusing on significant erosion areas such as the pressure side and blade edge, through the introduction of surface roughness.

Initially, the computational domain adopts the MRF model for solution, enabling steady-state simulation of each region at different rotation or movement speeds. The computational domain is discretized into multiple smaller subdomains, where governing equations are solved independently within each subdomain. Exchange of flow field information between subdomains is facilitated at their interfaces through velocity conversion into absolute velocity. Finally, while maintaining other boundary conditions constant, simulations are conducted at a propeller rotational speed of 1000 r/min and a cruise speed of 57.3 m/s.

Figure 15 illustrates the computed static pressure distribution and vorticity contour map on the blade surface, revealing a noticeable upward development of the blade tip vortex. Figure 16 depicts variations in the propeller thrust coefficient C_T and power coefficient C_P with roughness K_s under different operating conditions. It is evident that as roughness increases, both C_T and C_P display a declining trend when the blade edge and pressure side are uniformly roughened. At a roughness value of K_s = 500 μm, the power loss reaches 4.4%, indicating a proportional increase in the impact on the propeller's aerodynamic performance with roughness augmentation. When roughness is applied solely to the blade edge or pressure side, the influence on C_T and C_P is marginal (0.3%) at K_s = 500 μm for the former, and

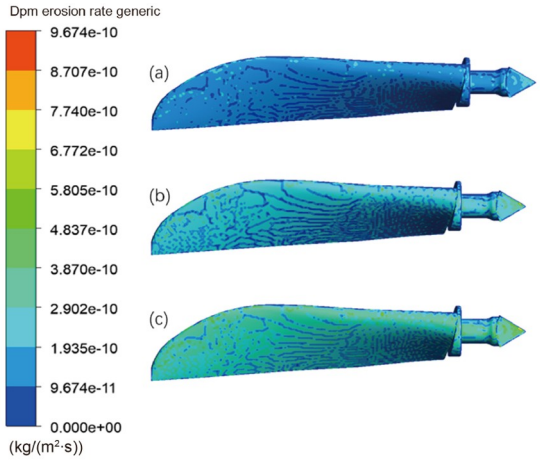

Figure 13 Different mass flow rates: (a) 0.5 kg/s; (b) 0.8 kg/s; (c) 1.0 kg/s.

nearly consistent with the scenario of roughening both the blade edge and pressure side for the latter. This comparison underscores the predominant role of pressure side roughness in affecting the propeller's power.

4. Conclusions

This paper addresses the erosion phenomenon experienced by propeller blades operating in harsh wind-sand environments, such as deserts and plateaus, and delves into the influence of sand dust particles on propeller erosion, along with its subsequent impact on propeller aerodynamic characteristics. Utilizing numerical simulation techniques, the study investigates propeller operational parameters (climb angle, rotational speed), the effects of particle parameters (particle diameter, inlet velocity, mass flow rate), and various roughness-induced damages on propeller aerodynamic behavior.

(1) Examination of processed blade surface data reveals that erosion remains concentrated at the blade edge and pressure side in the investigation of propeller operational parameters. It is observed that as the climb angle increases,

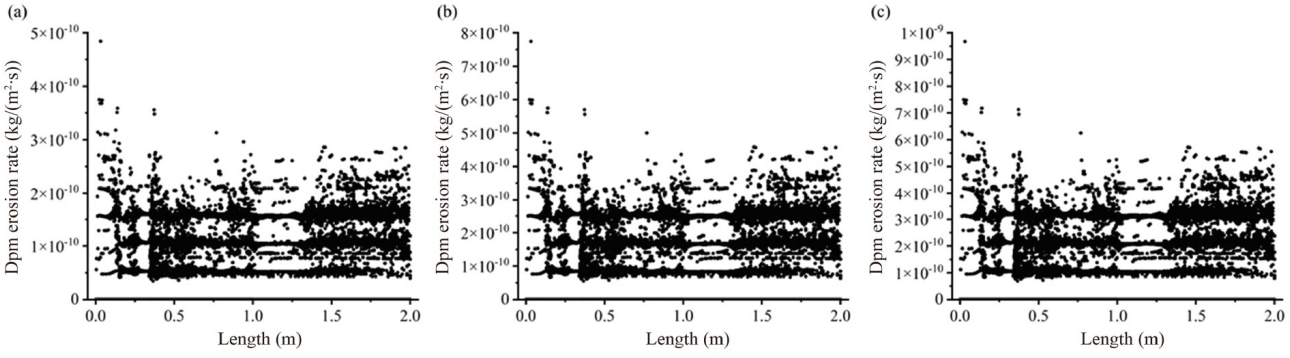

Figure 14 Scatterplot of erosion: (a) 0.5 kg/s; (b) 0.8 kg/s; (c) 1.0 kg/s.

Table 6 Average erosion rate: different mass flow rates

Mass flow rate (kg/s)	E_A (kg/(m^2·s))	Δ%
0.5	5.135014×10^{-11}	–
0.8	8.214178×10^{-11}	60%
1.0	1.026932×10^{-10}	100%

Table 7 Comparison of the effect of particle parameters on erosion rates

Parameter condition	Particle diameter	Incidence velocity	Mass flow rate
Condition 1	–	–	–
Condition 2	10.10%	0.20%	60%
Condition 3	12.70%	0.90%	100%

erosion extends gradually from the blade tip to the entire blade surface, resulting in an incremental enlargement of the erosion area and a corresponding reduction in overall erosion severity. Furthermore, with increasing rotational speed, the erosion area shifts from a scattered distribution to a concentration primarily at the blade edge and tip, with erosion severity intensifying.

(2) Comparative analysis of simulation results highlights that severe erosion predominantly occurs at the blade edge and tip under different particle parameter settings. An increase in particle size leads to a moderate decrease in the maximum erosion rate but an overall escalation in erosion severity. In addition, an increase in particle inlet velocity and mass flow rate is associated with an increase in both the maximum erosion rate and the overall severity of erosion. When comparing the effects of these two factors on erosion, it is observed that changes in mass flow rate have a particularly pronounced impact. Specifically, when the mass flow rate is increased to 1 kg/s, erosion is doubled compared to a mass flow rate of 0.5 kg/s. In contrast, the impact of changes in particle inlet velocity on erosion is negligible, as variations in velocity only result in approximately a 1% difference in erosion.

(3) The elucidation of propeller blade erosion patterns enhances the understanding of the impact on propeller performance. By introducing roughness (0-500 μm) to the pressure side and blade edge, simulation results demonstrate a degradation in propeller performance due to erosion-induced roughness. A roughness level of 500 μm leads to a performance loss of 4.4%, with roughness on the pressure side playing a predominant role in the degradation process.

The investigation into propeller erosion patterns in wind-

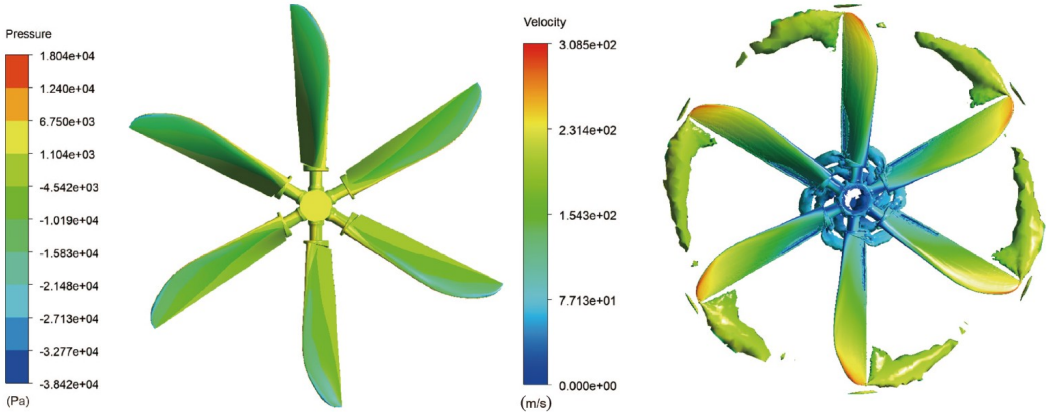

Figure 15 Propeller blade pressure distribution and vortex distribution.

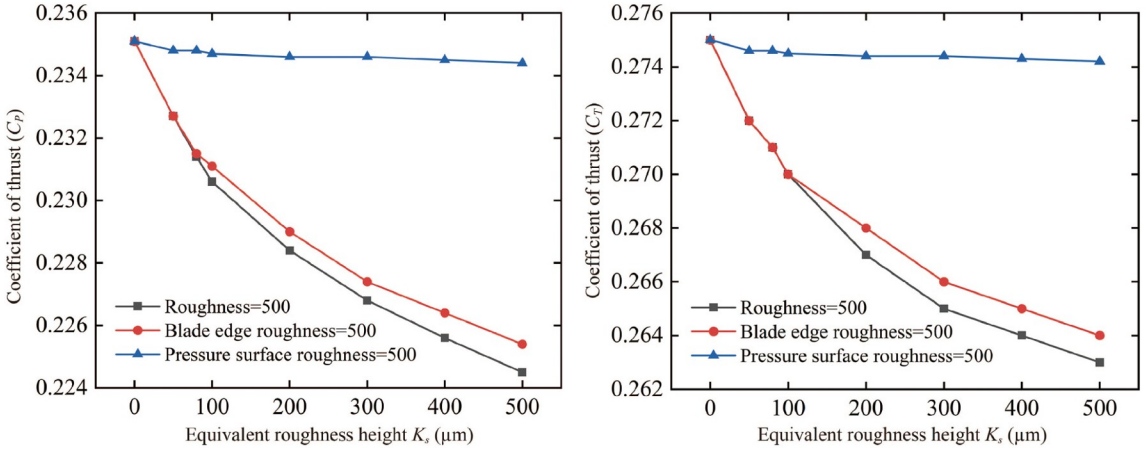

Figure 16 Power coefficients and thrust coefficients for different roughness cases.

sand environments facilitates targeted design, control, and optimization strategies, offering a robust theoretical foundation for ensuring the stable operation of new aircraft during flight.

Conflict of interest *On behalf of all authors, the corresponding author states that there is no conflict of interest.*

Author contributions *Xiangying Guo designed the research. Xiangying Guo and Fujin Zang wrote the first draft of the manuscript. Dongxing Cao set up the experiment set-up and processed the experiment data. Yunan Zhu helped organize the manuscript. Xiangying Guo and Dongxing Cao revised and edited the final version*

Acknowledgements *This work was supported by the National Natural Science Foundation of China (Grant Nos. 12172014, U2241264, and 12332001), and the National Key Laboratory of Helicopter Aeromechanics Fund (Grant No. 61422202206).*

1 M. Pepi, R. Squillacioti, L. Pfledderer, and A. Phelps, Solid particle erosion testing of helicopter rotor blade materials, J. Fail. Anal. Preven. **12**, 96 (2012).
2 T. Nicholas, J. P. Barber, and R. S. Bertke, Impact damage on titanium leading edges from small hard objects, Exp. Mech. **20**, 357 (1980).
3 I. M. Hutchings, A model for the erosion of metals by spherical particles at normal incidence, Wear **70**, 269 (1981).
4 Y. I. Oka, and T. Yoshida, Practical estimation of erosion damage caused by solid particle impact, Wear **259**, 102 (2005).
5 B. G. Shin, Prediction of Sand Particle Trajectories and Sand Erosion Damage on Helicopter Rotor Blades (The Pennsylvania State University, Pennsylvania State, 2010).
6 Z. G. Liu, S. Wan, V. B. Nguyen, and Y. W. Zhang, in Finite element analysis of erosive wear for offshore structure: Proceedings of 13th International Conference on Fracture, 2013.
7 A. P. Harsha, U. S. Tewari, and B. Venkatraman, Solid particle erosion behaviour of various polyaryletherketone composites, Wear **254**, 693 (2003).
8 B. Öztürk, H. Gedikli, and Y. S. Kılıçarslan, Erosive wear characteristics of E-glass fiber reinforced silica fume and zinc oxide-filled epoxy resin composites, Polym. Compos. **41**, 326 (2020).
9 N. H. Arani, W. Rabba, and M. Papini, Solid particle erosion of epoxy matrix composites reinforced by Al_2O_3 spheres, Tribol. Int. **136**, 432 (2019).
10 A. Purohit, A. Satapathy, P. Tapas Ranjan Swain, and P. Kumar Patnaik, A study on erosion wear behavior of ld sludge reinforced polypropylene composite, Mater. Today-Proc. **18**, 4299 (2019).
11 P. H. Usha Rani, B. M. Rajaprakash, N. Mohan, and M. Akshay Prasad, Study on thermal and erosive wear behaviour of hard powders filled glass-epoxy composite, Mater. Today-Proc. **27**, 2011 (2020).
12 İ. Özen, H. Gedikli, and B. Öztürk, Improvement of solid particle erosion resistance of helicopter rotor blade with hybrid composite shield, Eng. Fail. Anal. **121**, 105175 (2021).
13 C. Li, G. Bin, J. Li, and Z. Liu, Study on the erosive wear of the gas-solid flow of compressor blade in an aero-turboshaft engine based on the Finnie model, Tribol. Int. **163**, 107197 (2021).
14 C. Li, G. Bin, J. Li, P. Yang, and W. Wang, Influence of inlet distortion on the wear of aero-compressor blades, Int. J. Mech. Sci. **230**, 107551 (2022).
15 C. Li, G. Bin, J. Li, and P. Yang, Erosion wear characteristics of the aero-compressor blades in full speed range, Powder Tech. **418**, 118227 (2023).
16 A. Ghenaiet, S. C. Tan, and R. L. Elder, Prediction of an axial turbomachine performance degradation due to sand ingestion, Proc. Inst. Mech. Eng. Part A-J. Power Energy **219**, 273 (2005).
17 X. Dong, Z. Li, L. Feng, Z. Sun, and C. Fan, Modeling, simulation, and analysis of the impact(s) of single angular-type particles on ductile surfaces using smoothed particle hydrodynamics, Powder Tech. **318**, 363 (2017).
18 X. Dong, G. Liu, Z. Li, and W. Zeng, A smoothed particle hydrodynamics (SPH) model for simulating surface erosion by impacts of foreign particles, Tribol. Int. **95**, 267 (2016).
19 M. Suzuki, and M. Yamamoto, Numerical simulation of sand erosion phenomena in a single-stage axial compressor, J. Fluid Sci. Technol. **6**, 98 (2011).
20 K. Wood, Blade repair: Closing the maintenance gap, Compos. Technol. **9**, (2011).
21 A. Corsini, A. Castorrini, E. Morei, F. Rispoli, F. Sciulli, and P. Venturini, Modeling of rain drop erosion in a multi-MW wind turbine: Proceedings of the ASME Turbo Expo 2015: Turbine Technical Conference and Exposition, Montreal, 2015.
22 M. J. Tobar, J. M. Amado, C. Álvarez, A. García, A. Varela, and A. Yáñez, Characteristics of Tribaloy T-800 and T-900 coatings on steel substrates by laser cladding, Surf. Coatings Tech. **202**, 2297 (2008).
23 A. V. Ryzhenkov, S. I. Pogorelov, N. A. Loginova, E. V. Belyaeva, and A. Y. Plestsheva, Syntactic foams efficiency with the use of various microspheres for heat supply equipment and pipelines heat insulation, Modern Appl. Sci. **9**, 85 (2015).
24 K. L. Edwards, and C. Davenport, Materials for rotationally dynamic components: rationale for higher performance rotor-blade design, Mater. Des. **27**, 31 (2006).
25 X. Bai, Y. Yao, Z. Han, J. Zhang, and S. Zhang, Study of solid particle erosion on helicopter rotor blades surfaces, Appl. Sci. **10**, 977 (2020).
26 Z. X. Chen, H. X. Hu, X. M. Guo, and Y. G. Zheng, Effect of groove depth on the slurry erosion of V-shaped grooved surfaces, Wear **488-489**, 204133 (2022).
27 Z. Zhang, F. Li, L. Cao, P. Hu, and Y. Li, Research on characteristics of solid particle erosion in governing stage of a 600 MW supercritical steam turbine, Appl. Thermal Eng. **118**, 471 (2017).
28 G. G. Chochua, and S. A. Shirazi, A combined CFD-experimental study of erosion wear life prediction for non-Newtonian viscous slurries, Wear **426-427**, 481 (2019).
29 Z. Wang, J. Zhang, S. A. Shirazi, and Y. Dou, Predicting erosion in a non-Newtonian shear-thinning jet flow with validated CFD models from PIV and PTV measurements, Wear **426-427**, 501 (2019).
30 Z. A. Majid, R. Mohsin, and M. Z. Yusof, Experimental and computational failure analysis of natural gas pipe, Eng. Fail. Anal. **19**, 32 (2012).
31 M. Azimian, and H. J. Bart, Computational analysis of erosion in a radial inflow steam turbine, Eng. Fail. Anal. **64**, 26 (2016).
32 T. Alam, and Z. N. Farhat, Slurry erosion surface damage under normal impact for pipeline steels, Eng. Fail. Anal. **90**, 116 (2018).
33 G. I. Ilieva, Erosion failure mechanisms in turbine stage with twisted rotor blade, Eng. Fail. Anal. **70**, 90 (2016).
34 A. Evstifeev, N. Kazarinov, Y. Petrov, L. Witek, and A. Bednarz, Experimental and theoretical analysis of solid particle erosion of a steel compressor blade based on incubation time concept, Eng. Fail. Anal. **87**, 15 (2018).
35 C. Yan, W. Chen, and Z. Zhao, Experimental study on the high-speed impact of a sand particle on Ti-6Al-4V, Proc. Inst. Mech. Eng. Part J-J. Eng. Tribol. **234**, 632 (2020).
36 J. Alqallaf, and J. A. Teixeira, Numerical study of effects of solid particle erosion on compressor and engine performance, Results Eng. **15**, 100462 (2022).
37 R. Kyle, F. Wang, and B. Forbes, The effect of a leading edge erosion shield on the aerodynamic performance of a wind turbine blade, Wind Energy **23**, 953 (2020).
38 R. Roul, and A. Kumar, Fluid-structure interaction of wind turbine blade using four different materials: Numerical investigation, Symmetry **12**, 1467 (2020).

39 C. Kamble, S. S. Girimaji, and H. C. Chen, Partially averaged Navier-Stokes formulation of a two-layer turbulence model, AIAA J. **58**, 174 (2020).
40 İ. Özen, and H. Gedikli, Solid particle erosion on shield surface of a helicopter rotor blade using computational fluid dynamics, J. Aerosp. Eng. **32**, 04018131 (2019).
41 G. P. Tilly, Erosion caused by impact of solid particles, Treatise Mater. Sci. Technol. **13**, 287 (1979).

飞机螺旋桨冲蚀磨损及气动学特性

郭翔鹰, 臧富瑾, 朱雨男, 曹东兴

摘要 本文研究了螺旋桨运输机在沙漠、高原等恶劣环境中飞行时, 螺旋桨与沙尘颗粒碰撞和摩擦引起的表面冲蚀磨损. 首先, 使用商业软件FLUENT分析在不同沙尘颗粒参数下单个螺旋桨叶片的冲蚀行为. 随后, 通过滑移网格法对整个叶片进行动态模拟, 研究在不同工况条件下(包括转速和爬升角度)的冲蚀机理. 最后, 根据模拟结果, 得出冲蚀对螺旋桨气动特性的影响. 该研究深入探讨了大型飞机螺旋桨在沙尘环境中运行时的冲蚀规律以及螺旋桨表面冲蚀磨损对气动性能的影响. 通过阐明这些现象, 本研究为未来优化螺旋桨设计提供了宝贵的意见.